Proceedings 10th NUMGE 2023
10th European Conference on Numerical Methods in Geotechnical Engineering
Zdravkovic L, Kontoe S, Taborda DMG, Tsiampousi A (eds)

https://doi.org/10.53243/NUMGE2023-261

Influence of initial confining stress on the quasi-steady state

S.U.U.S. Shah, R. Cudmani, A.A. Peña-Olarte

Zentrum Geotechnik, Technical University of Munich, Munich, Germany

ABSTRACT: In the laboratory, the minimum mobilized undrained shear resistance (at the quasi-steady state, QSS) of sand samples consolidated to the same void ratio (e) has been found to be dependent on the initial confining pressure (p'_c). This non-uniqueness of the QSS is investigated in this paper using the DEM with the aim to understand its governing micromechanics. Similar to the experiments, the results of the numerical simulations showed a peak followed by a drop in the shear resistance to a minimum value at the QSS. Further shearing led to an increased regain of the shear resistance towards the steady state (SS). Up to the QSS, the rate of decrease of mean effective pressure and average coordination number increased with the decreasing p'_c values. This can be attributed to the increasing proportion of sliding contacts with the decreasing p'_c at a given axial strain which suggests the correspondingly increasing particle rearrangement at the QSS with the decreasing p'_c. At the QSS, contacts between the coarser and finer sized grain fractions showed negligible contribution to the overall strength but this contribution increased with the increasing p'_c.

Keywords: Undrained strength; Quasi-steady state; Coordination number

1 INTRODUCTION

In soil mechanics, liquefaction is a phenomenon of substantial strength loss under undrained shearing conditions. Literature shows a large number of undrained tests on the loose sandy samples undergoing large and rapid strength reduction accompanied by the rapid deformations (Castro et al., 1982; Been et al., 1991; Yamamuro and Lade, 1998). This loss in strength is related to the reduction in the effective stresses due to the contractive tendency of a loose granular skeleton. This concept of liquefaction has been systematically presented within the framework of the steady state (SS), which is defined as the ultimate state at which a sample deforms with vanishing stress and volumetric strain rate (Been et al., 1991; Verdugo and Ishihara, 1996). In addition to the steady state (or critical state), the quasi-steady state (QSS), which is a state of minimum resistance mobilized during undrained shearing, has also been consistently observed (Alarcon-Guzman et al., 1988; Been et al., 1991; Ishihara, 1993; Verdugo and Ishihara, 1996; Yamamuro and Lade, 1998; Murthy et al., 2007). Furthermore, according to Jefferies and Been (2015), once the state of instability (which is marked by the initial and rapid peak in strength) is passed, the strength drop can result in a rapid flowslide. Sladen et al. (1985) and Zhang and Garga (1997) doubted whether the post-QSS hardening is actually a feature of granular soil behaviour or resulting from some experimental artefact.

Therefore, it is more recommendable to use this lowest strength instead of the generally higher strength at the SS for the purpose of liquefaction analysis, also because it is mobilized at relatively small levels of strains. Ishihara (1993) presented undrained triaxial test results on Toyoura sand (a sub-angular grained quartz sand) sheared at the same void ratio (e) but different p'_c. Their results suggest that the pressure corresponding to the QSS increases with the increasing p'_c. Konard (1993) presented triaxial undrained tests on Hostun RF sand (a sub-angular grained quartz sand) for very loose states and also showed the effective stress at the QSS to be increasing with the p'_c within a narrow range of e. Figure 1 shows the state points (initial and at the steady state) for a tailing sand (predominantly siliceous with angular grains) tested by Fourie and Tshabalala, (2005). As can be seen, for a very narrow range of e, the mean effective stress mobilized at the QSS increased with the increase in p'_c.

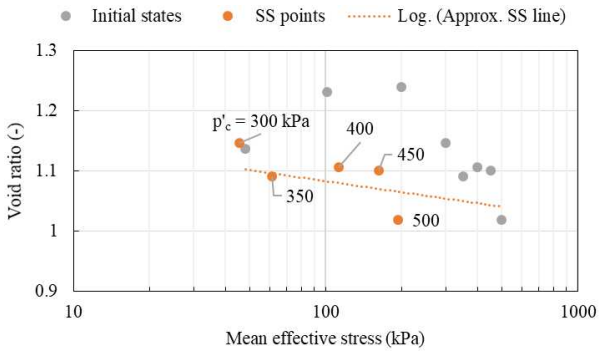

Figure 1. State points of a tailing sand with data labels showing the initial consolidation pressure of each test (data replotted after Fourie and Tshabalala, 2005)

Similar p'_c depedency can be observed in undrained triaxial tests on Syncrude tailing sand (quartz sand with

angular grains) presented by Sladen and Hanford (1987). This paper employs discrete element modelling (DEM) using the PFC3D program (Itasca Consulting Group, Inc. 2021) to investigate the p'_c dependence of the QSS from the micromechanical point of view.

2 BRIEF MODELLING METHODOLOGY

The simulated particle size distribution (PSD) is the same as that modelled by Huang et al. (2014) and Perez et al. (2016) with the mean particle diameter (D_{50}) of 0.22 mm and the coefficient of uniformity (C_u) of 1.6 (Figure 2). The scheme of periodic boundaries after Thornton (2000) was implemented for homogeneity within the samples and to avoid the dilation induced by rigid boundaries as shown in Huang et al. (2014). Initially cubical samples composed of 10,000 polyhedral particles were simulated having in view the eccentric and complex nature of real sand grains (Yang and Luo, 2015; Zheng and Hryciw, 2016; Yang et al., 2019). Moreover, Lee at al. (2012) showed the DEM simulations using simple polyherdral shaped particles to be reproducing the contractive-dilative behaviour of a real sand. In order to avoid very high computational demand due to the contact searching and resolution, the number of grain facets was restricted to eight. Another reason to opt for rather simplified grain geometries is the manifold and complex morphology of real sand grains which is extremely difficult to capture let alone modelling it (Nguyen et al., 2021). Deformability method with linear force-displacement formulation was used at the contacts. Due to the space limitations, the details of this contact model are not given here and can be seen in Potyondy and Cundall (2004). This formulation scales contact stiffness with respect to the size of contacting bodies, which can be corroborated with the contact-level laboratory tests from Sandeep et al. (2021). The notable model parameters used are: effective contact modulus (E) = 1.1x10^8 N/m^2, ratio of normal to shear contact stiffness (κ) = 1.5, inter-particle sliding friction coefficient (μ) = 0.34 and critical (normal and shear) damping ratio (β) = 0.2. The notional particle density of 3356 kg/m^3 was used and the gravity was not simulated. Density scaling was also done in order to get longer integration time increments which is common in modelling realm (O'Sullivan, 2011). The unbalanced force ratio, as defined by the ratio between the average unbalanced force to the average contact force acting on each particle, reflects the state of equilibrium. Following the constant-volume simulations from Barnett et al. (2021), the average unbalanced force ratio of less than 10^{-4} was ensured in all simulations. During the genesis of assembly, the inter-particle friction coefficient was varied to get different initial void ratio and corresponding isotropic compression paths. Notionally undrained (constant-volume) simulations were performed by prescribing the strain rates in both minor principal strain direction to be half and opposite to the vertical (major prinicipal direction) strain rate . The stress tensor was computed according to Equation (1), as suggested by Christoffersen et al. (1981) which is commonly utilized in the DEM studies.

$$\sigma'_{ij} = \frac{1}{V}\sum_{1}^{N_c} \boldsymbol{f}_i \boldsymbol{l}_j \qquad (1)$$

where N_c is the number of contacts inside the measurement region of volume V, $\boldsymbol{f}_i$ is the contact force vector and $\boldsymbol{l}_j$ is the branch vector (vector joining the centroid of two contacting pieces). i and j cycle from 1-3 (3-dimensions). Equation (1) takes outer product between the contact force vector and the branch vector. Void ratio (e) was calculated within the periodic domain. Initial state parameter (Ψ_o) was taken as the difference between e and e at the SS corresponding to the p'_c. Used stress invariants are $q = \sigma'_{33} - \sigma'_{11}$ and $p' = (\sigma'_{33} + 2\sigma'_{11})/3$. Where, σ'_{33} and σ'_{11} are the major and minor principal stresses, respectively. Furthermore, $\sigma'_{11} = \sigma'_{22}$ due to the considered axisymmetry.

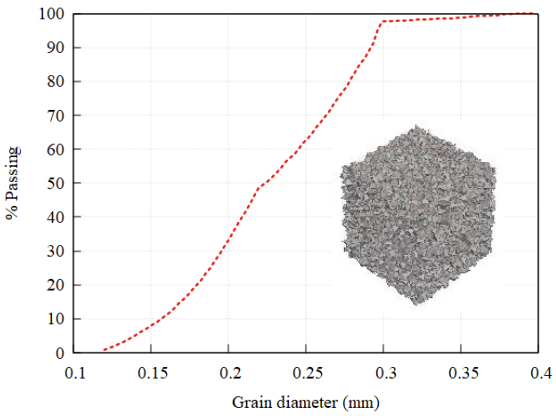

Figure 2. Grain size distribution and the virgin sample

3 RESULTS AND DISCUSSION

Figure 3 shows three selected simulations from the isotropic consolidation lines (ICLs) lying above and below the steady-state line (SSL). The SS points are plotted including various other simulations at the variety of states. The SSL approximated with the power-law function is shown in Equation (2). The reasonability of such approximation is shown in Li and Wang (1998); Murthy et al. (2007); Yang and Lo (2015), etc.

$$e_{ss} = \Gamma - \lambda.\left(p'/p'_a\right)^{\xi} \qquad (2)$$

where p'_a is the atmospheric pressure, and Γ, λ and ξ are the fitting parameters. Γ indicates the intercept of SS

line with void ratio axis upon vanishing stresses and λ shows its slope on $e-(p'/p'_a)^{\xi}$ plane. The performed regression resulted the values of Γ, λ and ξ to be 0.73, 0.017 and 0.625, respectively.

In the following subsections, the macro- and micro-mechanics of three samples sheared at the same e but different p'_c will be discused.

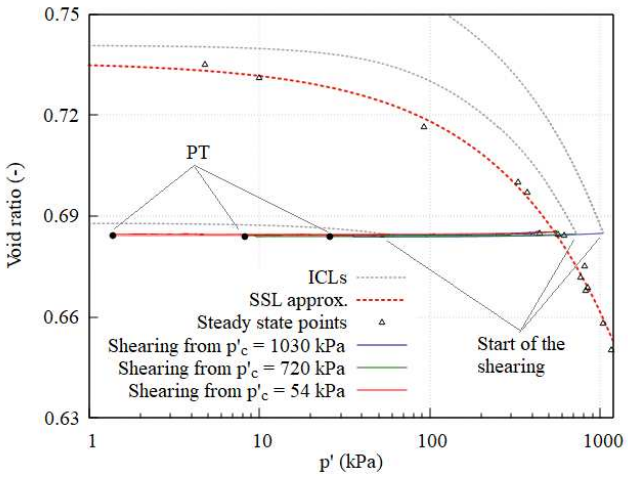

Figure 3. Simulated states along with the isotropic consolidation lines (ICLs), steady state line (SSL) and their phase transformation (PT) points.

3.1 Macro-mechanical evolutions

Figure 4 shows the deviator stress vs. axial strain for three samples sheared at the same e but different consolidation pressures p'_c. After the start of shearing, the inital peak strength (or instability state) was mobilized at relatively small axial strain followed by softening until the quasi-steady state (where temporarily $\delta q = 0$). Further shearing beyond the QSS led to the hardening of samples until the condition of $\delta q = \delta p' = 0$ (steady or cirtical state) was reached. Both, the axial strains corresponding to the peak state and QSS and the strain range between the peak state and QSS increased with the increasing p'_c. These observations are consistent with the experimental results from foregoing investigations.

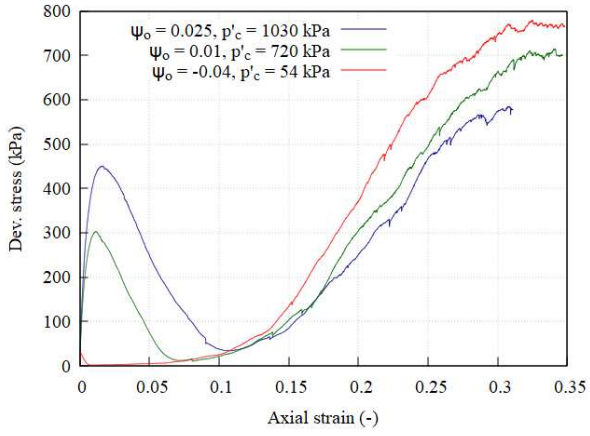

Figure 4. Stress-strain curves

Figure 5 shows the deviator stress vs. mean normal stress for the three samples in discussion. The p' decreased monotonically until the QSS followed by an increase towards the SS. Points of instability can be observed in this plot as corresponding to the initial peak in q followed by the pronounced softening. Therefore, the points of instability mark the triggering of the softening.

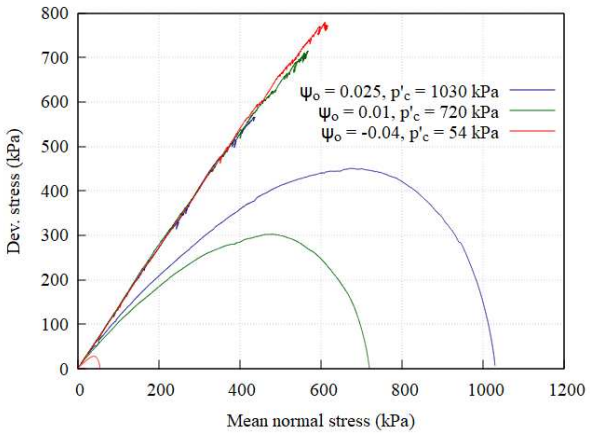

Figure 5. Deviator stress vs. mean normal stress

Until the SS, the deviatoric stress evolution was influenced by the p'_c. Even though shearing beyond the QSS showed different re-hardening stiffnesses (although non-linear) of the samples but the q/p' ratio stayed approximately constant and same in all samples.

3.2 Micro-mechanical evolutions

In this section, the micro-mechanical evolutions in samples during the shearing will be explained. The Coordination number (CN) is defined as the average number of contacts per particle. As each contact is being shared between two particles, the number of particles is halved as following:

$$Coordination\ number\ (CN) = {}^{2N_C}\!/_{N_p} \qquad (3)$$

where N_c is the number of contacts and N_p is the number of particles. In order to consider the redundancy of some particles that are observing either none or just one contact at an instance, the mechanical coordination number was proposed by Thornton (2000) as defined in Equation (4).

$$CN_{mech.} = {}^{(2N_c - N_p^1)}\!/_{(N_p - N_p^1 - N_p^0)} \qquad (4)$$

where N_p^0 and N_p^1 are the number of particles with zero or one contact, respectively. Figure 6 shows the evolution of average $CN_{mech.}$ vs. axial strain. After the start of shearing, the avg. $CN_{mech.}$ decreased until the QSS followed by an increase until the SS. The post-QSS

rate increase of $CN_{mech.}$ became higher with the decreasing p'_c until it achieved somewhat same value at the SS regardless of the p'_c. The rate of reduction of $CN_{mech.}$ until the QSS increased with decreasing p'_c which shows a faster reduction in the number of contacts with the decreasing p'_c.

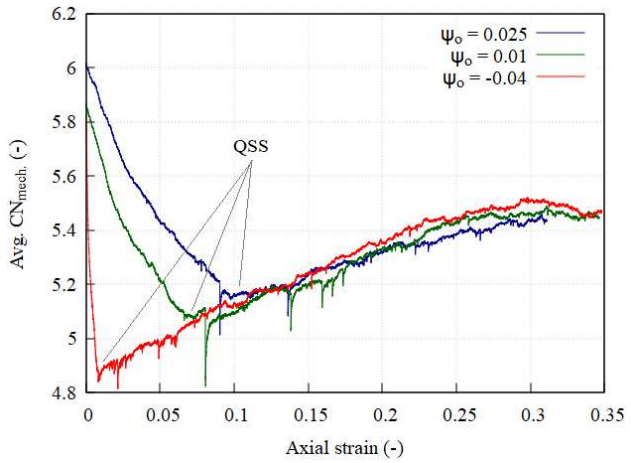

Figure 6. Average mechanical coordination number vs. axial strain

Eventhough the strength achieved after the QSS exceeded the strength at instability, the avg. $CN_{mech.}$ stayed lower than its inital value which indicates the post-liquefaction strengthning of contacts.

Fabric is defined in the form of a second rank tensor as proposed by Satake (1978) in Equation (5). This definition of fabric is extensively used in DEM research.

$$Fabric\ tensor\ = \varphi_{ij} = \frac{1}{N_c}\sum_{1}^{N_c} \boldsymbol{n}_i \boldsymbol{n}_j \qquad (5)$$

where $\boldsymbol{n}$ is the contact normal unit vector with $\boldsymbol{n}_i$ and $\boldsymbol{n}_j$ being the corresponding column and row vectors, respectively. The evolution of fabric deviator ($\varphi_d = \varphi_{33} - \varphi_{11}$) is shown in Figure 7. $\varphi_{22} = \varphi_{11}$ due to the assumed transverse-isotropy. For all the three samples, the fabric deviator evolved continously throughout the shearing. As can be seen in Figure 7, the φ_d increased until the phase transformation (where temporarily $\delta p' = 0$). The φ_d evolved rapidly during the phase transformation. This indicates that a larger fraction of contact normals started aligning in the major principal stress direction while p' was reducing towards its minimum value. The fabric deviator achieved a nearly constant value (i.e. $\delta\varphi_d \approx 0$) at the SS, which was independent of the p'_c. It can be seen that until the QSS, the $\delta\varphi_d/||\delta p'||$ decreased with the increasing p'_c. This indicates that smaller the p'_c, the faster the reorientation of contact normals. Figure 8 shows the fraction of sliding contacts, i.e. ratio of the number of contacts for which contact tangent force magnitude = μ.(contact normal force) to the N_c, as a function of axial strain. The rapid increase of sliding contacts indicates sudden particles rearrangement at the beginning of shearing. The QSS conincides with the point at which the fraction of sliding contacts achieves a maximum. Although the increase in the fraction of sliding contacts happened untill the QSS in all of the samples, but a rapid increase happened untill the instability. This behaviour can be corroborated with the undrained counterpart of it which was named as structural collapse by Alarcon-Guzman et al. (1988). According to this hypothesis, the metastable and loose grain assembly reacts to even slight boundary strains by a sudden rearrangement of grains and the loss of contacts between neighbouring grains. Consequently, a rapid development of excess pore water pressure occurs as the interstitial water has very low compressibility and the drainage is not permitted.This mechanism invovles the loss of effective stress and hence the strength which reaches a plateau near the QSS followed by a dilative response. In Figure 8, for shearing beyond the QSS, the fraction of sliding contacts is reducing with somewhat the same rate for all the samples and the contacts are getting stronger (increase in the macro-mechanical stresses). Furthermore, sharp fluctuations can be seen in the fraction of sliding contacts, which point to the stick-slip mechanism (interplay between the frictional sticking/jamming and grain rearrangement) which, until

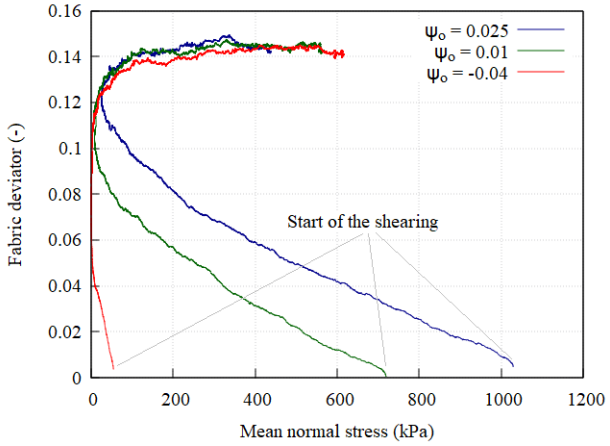

Figure 7. Fab deviator vs. mean normal stress

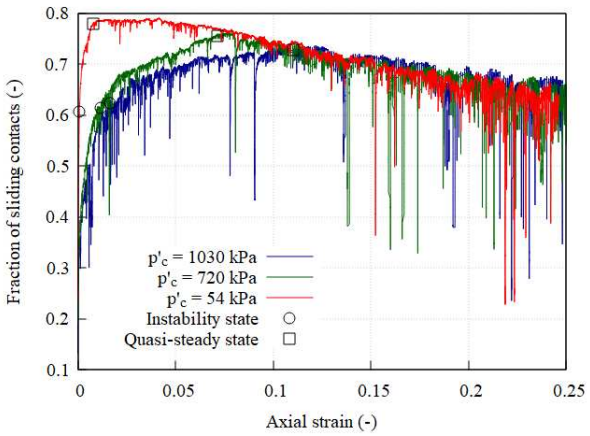

Figure 8. Fraction of sliding contacts vs. axial strain

the QSS, became prominent with the increase in p'_c. Shearing beyond the QSS showed stronger stick-slip features in all samples, which points to the more frequent formation and buckling of strong force-chains.

Equation (6) shows the decomposition of stress tensor in order to observe the contribution from different particle size fractions to the overall strength. Similar decomposition of stress tensor was also performed by Dai et al. (2015) but their attained initial states were extreme enough to show either the full liquefaction or the phase transformation without the presence of the quasi-steady state.

$$\sigma'_{ij} = \sigma'^{c-c}_{ij} + \sigma'^{c-f}_{ij} + \sigma'^{f-f}_{ij} \qquad (6)$$

where the superscripts *c-c*, *c-f* and *f-f* refer to the coarse-to-coarse, coarse-to-fine and fine-to-fine particle contacts, respectively. Here, the percentage passing of 10% (corresponding to the grain diameter of 0.156 mm) was arbitrary set to separate the coarse and the fine fractions. Interestingly, even though the fines were considered as 10% passing, they are half in number of the rest of the grains (coarser particles). Figure 9 (a-c) shows the dissociated deviatoric stresses for all the three sample. The contribution from *f-f* grain contacts to the overall stress wass negligible but increased relatively after the QSS. The stresses from *c-c* grain contacts consituted a major portion of the overall strength and *c-f* particle contacts had vanishing contribution upon the QSS and showed recontributing from then on (until the SS). It can be seen that the QSS coincides with a temporary but substantial reduction of stress contribution from contacts. As can be seen in the Figure 9 (a-c), the lower the p'_c, the more prominent was the reduction in deviatoric stressed from the *c-f* and *c-c* grain contacts.

4 CONCLUSIONS

Based on the results of axisymmetric constant volume compression tests on idealized assemblies, it can be concluded that the quasi-steady state is assembly's own behaviour which originates from granular rearrangement. As expected, the existence of the SS is confirmed by DEM simulations. Regarding the QSS, this investigation did not only confirm the macroscopic behaviour observed in the laboratory, but also shed light on the micromechanical behaviour upon liquefaction. The DEM simulations strengthen the laboratory-based observation that the mean effective stress mobilized at the quasi-steady state increases with the increase in consolidation pressure. The average coordination number showed the behaviour similar to the effective stress, i.e. decrease until the QSS and increase thereafter towards a constant value at the SS. The average coordination number at the QSS slightly increased with the consolidation pressure

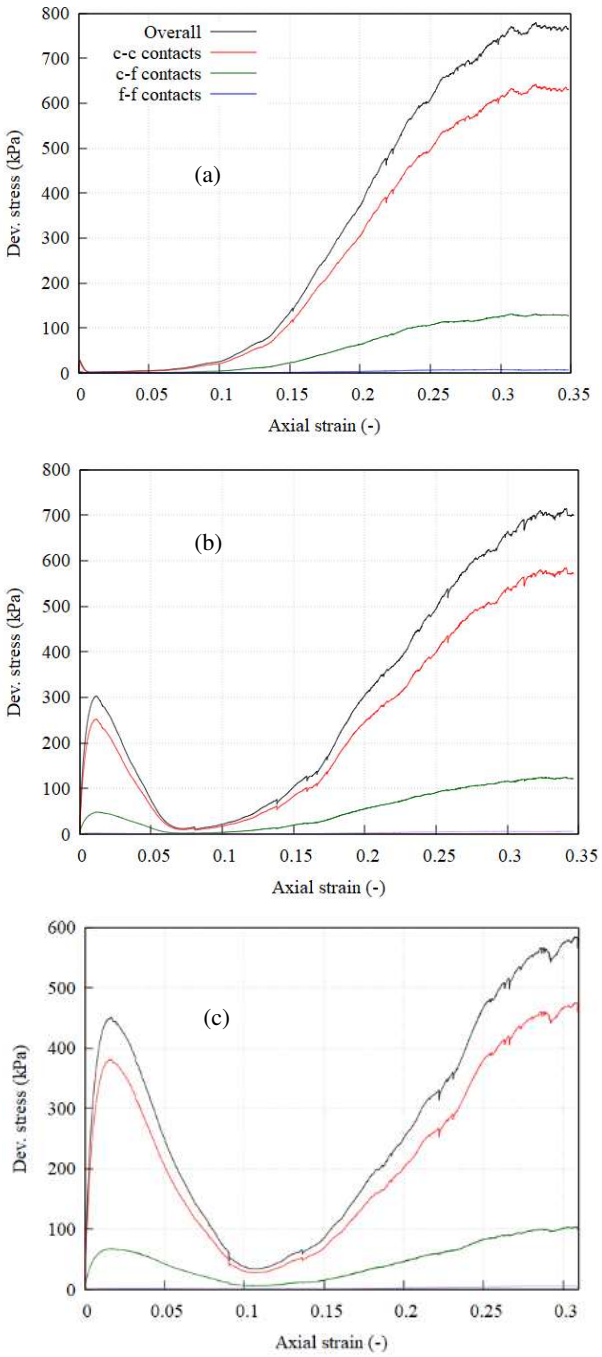

Figure 9. Dev. stress vs. axial strain for samples with p'_c = 54 kPa (a), 720 kPa (b) and 1030 kPa (c)

and its initial rate of reduction increased with the decrease in consolidation pressure. The fabric deviator evolved rapidly at the onset of the quasi-steady state, i.e. an increasingly higher number of contact normals started aligning vertically (along the direction of major principal stress/strain). This rapid evolution was enhanced with the decrease in consolidation pressure. Until the QSS, the fraction of sliding contacts and its rate increased with decreasing consolidation pressure, which indicates higher rearrangement potential of assemblies at lower initial effective pressure. The dissociation of the stress tensor showed different strength contributions from the grain contacts depending on the size

of the particles being in contact. The major strength contribution resulted from the contacts between coarse particles, followed by the contacts between the coarse and fine particles. On the contrary, the strength contribution from the contacts between fine particles was negligible.

In the light of the laboratory tests (from literature) and simulations herein, the QSS's dependency on the consolidation pressure suggests that when the shear strength at the QSS is a concern, the initial stress level should also be given a due consideration in addition to the void ratio and the state parameter.

5 ACKNOWLEDGEMENTS

Authors are highly grateful to ITASCA Inc. and HEC-DAAD for the provision of computational program's license and financial support, respectively.

6 REFERENCES

Alarcon-Guzman, A., Leonards, G.A. and Chameau, J.L., 1988. Undrained monotonic and cyclic strength of sands. J. of Geotech. Engineering, 114(10), pp.1089-1109.

Barnett, N., Rahman, M.M., Karim, M.R., Nguyen, H.K. and Carraro, J.A.H., 2021. Equivalent state theory for mixtures of sand with non-plastic fines: a DEM investigation. Géotechnique, 71(5), pp.423-440.

Been, K., Jefferies, M.G. and Hachey, J., 1991. The critical state of sands. Geotechnique, 41(3), pp.365-381.

Castro, G., Enos, J.L., France, J.W. and Poulos, S.J., 1982. Liquefaction induced by cyclic loading. NASA STI/Recon Technical Report N, 83, p.13308.

Cho, G.C., Dodds, J. and Santamarina, C.J., 2006. Particle shape effects on packing density, stiffness, and strength: natural and crushed sands. J Geotechnical and Geoenvironmental engineering 132 (5): 591–602.

Christoffersen, J., Mehrabadi, M.M. and Nemat-Nasser, S., 1981. A Micromechanical Description of Granular Material Behavior. J. of Applied Mechanics, 48(2), p.339.

Dai, B., Yang, J. and Luo, X., 2015. A numerical analysis of the shear behavior of granular soil with fines. Particuology, 21, pp.160-172.

Huang, X., Hanley, K.J., O'Sullivan, C. and Kwok, C.Y., 2014. Exploring the influence of interparticle friction on critical state behaviour using DEM. International Journal for Numerical and Analytical Methods in Geomechanics, 38(12), pp.1276-1297.

Ishihara, K., 1993. Liquefaction and flow failure during earthquakes. Geotechnique, 43(3), pp.351-451.

Itasca Consulting Group, Inc. 2021. PFC — Particle Flow Code, Ver. 7.0. Minneapolis: Itasca.

Jefferies, M. and Been, K., 2015. Soil liquefaction: a critical state approach. CRC press.

Konrad, J.M., 1993. Undrained response of loosely compacted sands during monotonic and cyclic compression tests. Géotechnique, 43(1), pp.69-89.

Lee, S.J., Hashash, Y.M. and Nezami, E.G., 2012. Simulation of triaxial compression tests with polyhedral discrete elements. Computers and Geotechnics, 43, pp.92-100.

Li, X.S. and Wang, Y., 1998. Linear representation of steady-state line for sand. Journal of geotechnical and geoenvironmental engineering, 124(12), pp.1215-1217.

Murthy, T.G., Loukidis, D., Carraro, J.A.H., Prezzi, M. and Salgado, R., 2007. Undrained monotonic response of clean and silty sands. Géotechnique, 57(3), pp.273-288.

Nguyen, H.B.K., Rahman, M.M. and Fourie, A.B., 2021. How particle shape affects the critical state, triggering of instability and dilatancy of granular materials–results from a DEM study. Géotechnique, 71(9), pp.749-764.

O'Sullivan, C., 2011. Particulate discrete element modelling: a geomechanics perspective. CRC Press.

Perez, J.L., Kwok, C.Y., Huang, X. and Hanley, K.J., 2016. Assessing the quasi-static conditions for shearing in granular media within the critical state soil mechanics framework. Soils and Foundations, 56, pp.152-9

Potyondy, D.O. and Cundall, P.A., 2004. A bonded-particle model for rock. International journal of rock mechanics and mining sciences, 41(8), pp.1329-1364.

Sandeep, C.S., Li, S. and Senetakis, K., 2021. Scale and surface morphology effects on the micromechanical contact behavior of granular materials. Tribology International, 159, p.106929.

Satake, M., 1978. Constitution of mechanics of granular materials through the graph theory. In Proc. US-Japan Seminar on Continuum Mech. Stat. Appr. Mech. Granul. Mater., Sendai (pp. 203-215)

Sladen, J.A. and Handford, G., 1987. A potential systematic error in laboratory testing of very loose sands. Canadian Geotechnical Journal, 24(3), pp.462-466.

Sladen, J.A., D'hollander, R.D. and Krahn, J., 1985. The liquefaction of sands, a collapse surface approach. Canadian geotechnical journal, 22(4), pp.564-578.

Thornton, C., 2000. Numerical simulations of deviatoric shear deformation of granular media. Géotechnique, 50(1), pp.43-53.

Verdugo, R. and Ishihara, K., 1996. The steady state of sandy soils. Soils and foundations, 36(2), pp.81-91.

Yamamuro, J.A. and Lade, P.V., 1998. Steady-state concepts and static liquefaction of silty sands. J. of geotechnical and geoenvironmental engineering, 124(9), pp.868-877.

Yang, J. and Luo, X.D., 2015. Exploring the relationship between critical state and particle shape for granular materials. J. of the Mech. and Physics of Solids, 84, pp.196-213.

Yang, Y., Wei, Z., Fourie, A., Chen, Y., Zheng, B., Wang, W. and Zhuang, S., 2019. Particle shape analysis of tailings using digital image processing. Environmental Science and Pollution Research, 26, pp.26397-26403.

Zhang, H. and Garga, V.K., 1997. Quasi-steady state: a real behaviour?. Can. Geot. Journal, 34(5), pp.749-76

Zheng, J. and Hryciw, R.D., 2016. Roundness and sphericity of soil particles in assemblies by computational geometry. Journal of Computing in Civil Engineering, 30(6), p.04016021.